PHYSICAL REVIEW B **97**, 064418 (2018)

Azimuthal spin-wave excitations in magnetic nanodots over the soliton background: Vortex, Bloch, and Néel-like skyrmions

M. Mruczkiewicz,[1,*] P. Gruszecki,[2] M. Krawczyk,[2] and K. Y. Guslienko[3,4]
[1]*Institute of Electrical Engineering, Slovak Academy of Sciences, Dubravska cesta 9, 841 04 Bratislava, Slovakia*
[2]*Faculty of Physics, Adam Mickiewicz University in Poznan, Umultowska 85, Poznań, 61-614, Poland*
[3]*Depatamento de Fisica de Materiales, Universidad del Pais Vasco, UPV/EHU, 20018 San Sebastian, Spain*
[4]*IKERBASQUE, the Basque Foundation for Science, 48013 Bilbao, Spain*

(Received 21 November 2017; published 21 February 2018)

We study azimuthal spin-wave (SW) excitations in a circular ferromagnetic nanodot in different inhomogeneous, topologically nontrivial magnetization states, specifically, vortex, Bloch-type skyrmion, and Néel-type skyrmion states. A continuous transition between these states is realized by gradually changing the out-of-plane magnetic anisotropy and the Dzyaloshinskii-Moriya exchange interaction (DMI), and the corresponding SW spectra are calculated for each state. We observe the lifting of degeneracy of SW mode frequencies and a change in the systematics of frequency levels. The latter effect is induced by the geometric Berry phase, which occurs in SWs localized at the edge of the dot in the vortex state, and vanishes in the skyrmion states. Furthermore, channeling of edge-localized azimuthal SWs and a related large frequency splitting are observed in the skyrmion states. This is attributed to DMI-induced nonreciprocity, while the coupling of the breathing and gyrotropic modes is related to the skyrmion motion. Finally, we demonstrate efficient coupling of the dynamic magnetization to a uniform magnetic field in nanodots of noncircular symmetry in the skyrmion states.

DOI: 10.1103/PhysRevB.97.064418

I. INTRODUCTION

Patterned magnetic nanostructures are considered for the construction of novel devices for information processing and storage [1,2] that could go beyond the limitations of semiconductor technology [3]. In particular, ultrathin magnetic structures with interface-induced Dzyaloshinskii-Moriya interaction (DMI) have become the subject of intensive research in this direction [4,5]. The DMI interaction energy is minimal when neighboring spins are perpendicular, with a specific sense of rotation. In this sense, the DMI implies chirality (handedness). With a sufficiently large contribution of the DMI to the total magnetic energy, the magnetization configuration in the ground state becomes inhomogeneous: spiral or skyrmion states occur. Such states are very promising for applications. For example, a skyrmion, considered as a stable nanometer-size topological magnetic soliton, can be manipulated by the application of low-energy external stimuli.

Although the DMI facilitates stabilization of inhomogeneous magnetization states, in a broad range of parameters (e.g., for low DMI strength or external magnetic field), the ground state is still a single-domain (SD) state [6,7]. However, even if the DMI does not change the static magnetization configuration, its influence on the magnetization dynamics is substantial. It has been shown that the DMI can affect the frequency of propagating spin waves (SWs) in the specific magnetization configuration in which the direction of SW propagation is perpendicular to the magnetization [8–10]. Also, the DMI breaks the symmetry of the SW dispersion relation by introducing nonreciprocity [$f(-k) \neq f(k)$]. This effect is commonly used for extracting the DMI strength from measured SW spectra.

DMI-induced nonreciprocity of SW propagation can also occur in confined-geometry systems. By numerical calculations and simulations, we have demonstrated SW nonreciprocity in magnetic nanostripes [11]. A modified spectrum of standing SWs and a significant increase in the coupling of quantized modes to a spatially uniform microwave field are predicted in an isolated stripe. Since reduction of the measurement time required for the determination of DMI strength is desired [12], this effect, if verified experimentally, would provide an alternative to Brillouin light scattering (BLS) for the estimation of DMI strength.

Spin-wave modes of various symmetry have been studied extensively in single-domain stripes [13,14], disks [15–25], ellipses [26–28], rings [29–35], and nanotubes [36]. Also the influence of the DMI on the stable magnetization state [37] and dynamic excitations has been investigated recently [6,9]. Spin-wave channeling in a domain wall has been demonstrated, opening the way to reconfigurable channels and controllable signal propagation [38,39]. Nonreciprocity and the DMI provide new degrees of freedom in the control of SWs [40]. Skyrmion dynamics has already been studied in circular geometry [41–50], but little attention has been paid so far to quantization of azimuthal SW modes. Since the magnetic configuration can favor nonreciprocity in many cases, the DMI can be expected to have a substantial influence on the spectrum of azimuthal SWs.

In this paper, we study the influence of the DMI on the localization and frequency of azimuthal SWs in a skyrmion magnetization background in a circular nanodot with the vortex as a

---

[*] mmruczkiewicz@gmail.com

reference state. We show that the topological Berry phase [51] lifts the degeneracy of dot edge-localized SWs and changes the systematics of eigenfrequencies. Moreover, by inducing nonreciprocity, the DMI causes frequency splitting between SWs with opposite directions of propagation, and leads to the creation of additional low-frequency quantized modes. We also demonstrate that the investigated magnetization configurations can be efficiently excited by a uniform microwave field in nanoelements with noncircular symmetry. Our results can be of use for controlling the magnetization dynamics in patterned nanostructures with DMI, SW channeling, and SW-controlled information processing.

II. MODEL

The physical system considered in this study is a thin circular ferromagnetic dot of thickness t and radius R. We determine its spectrum of spin excitations by performing finite difference time domain (FDTD) micromagnetic simulations using MUMAX^3 [52]. The calculations are based on the Landau-Lifshitz equation of motion of magnetization $\mathbf{M}$. The time derivative $\frac{\partial \mathbf{M}(\mathbf{r},t)}{\partial t}$ of the magnetization is defined as the torque τ, which can be expressed in the following form:

$$\tau = |\gamma| \frac{1}{1+\alpha^2}\left[\mathbf{M}\times\mathbf{B}_{\text{eff}} + \frac{\alpha}{M_s}(\mathbf{M}\times(\mathbf{M}\times\mathbf{B}_{\text{eff}}))\right], \quad (1)$$

where γ is the gyromagnetic ratio, α is a dimensionless damping parameter, M_{s} is the saturation magnetization, and $\mathbf{B}_{\text{eff}}$ is the effective magnetic field, which is the sum of the external magnetic field $\mathbf{B}_{\text{ext}}$, the magnetostatic field $\mathbf{B}_{\text{m}}$, the isotropic Heisenberg exchange field $\mathbf{B}_{\text{ex}}$ (proportional to the exchange stiffness constant A), the interface Dzyaloshinskii-Moriya exchange field $\mathbf{B}_{\text{DM}}$, and the uniaxial magnetocrystalline anisotropy field $\mathbf{B}_{\text{an}}$ (proportional to the uniaxial anisotropy constant K_{u}):

$$\mathbf{B}_{\text{eff}} = \mathbf{B}_{\text{ext}} + \mathbf{B}_{\text{m}} + \mathbf{B}_{\text{ex}} + \mathbf{B}_{\text{DM}} + \mathbf{B}_{\text{an}}. \quad (2)$$

Skyrmions in the dot are stabilized by an interplay between the isotropic exchange, DMI, uniaxial out-of-plane magnetic anisotropy, and magnetostatic energies, assuming zero bias magnetic field. According to Ref. [53], the DMI is implemented as an effective magnetic field:

$$\mathbf{B}_{\text{DM}} = \frac{2D}{M_{\text{s}}}\left(\frac{\partial m_z}{\partial x}, \frac{\partial m_z}{\partial y}, -\frac{\partial m_x}{\partial x} - \frac{\partial m_y}{\partial y}\right), \quad (3)$$

corresponding to the magnetic energy density:

$$\varepsilon = D(m_z(\nabla\cdot\mathbf{m}) - (\mathbf{m}\cdot\nabla)m_z), \quad (4)$$

where $\mathbf{m} = \mathbf{M}/M_{\text{s}}$ is the reduced magnetization vector, and D is the Dzyaloshinskii-Moriya interface exchange interaction constant.

Our simulations were performed in the following order. A Bloch skyrmion initial magnetization configuration was assumed first. In the next step, this initial state was relaxed in order to minimize the total magnetic energy of the system. As a result, the magnetic configuration could become a vortex, Bloch skyrmion or Néel skyrmion state, depending on the magnetic parameters (K_{u}, D) chosen. In most cases, the initial Bloch skyrmion state would relax to one of the ground states. However, for some combinations of the magnetic parameters of the dot, the Bloch skyrmion would become a metastable state and would not relax to a ground state. The corresponding parameter range is indicated in Fig. 1(a), where it is delimited by the white dashed line. In this case, a single-domain (SD) state could be used as the initial magnetization state for the system to relax to a ground state.

The stable magnetization configurations were excited by a low-amplitude variable magnetic field, the time dependence of which is represented by the function $\text{sinc}(2\pi f_{\max}(t-t_0))$, with

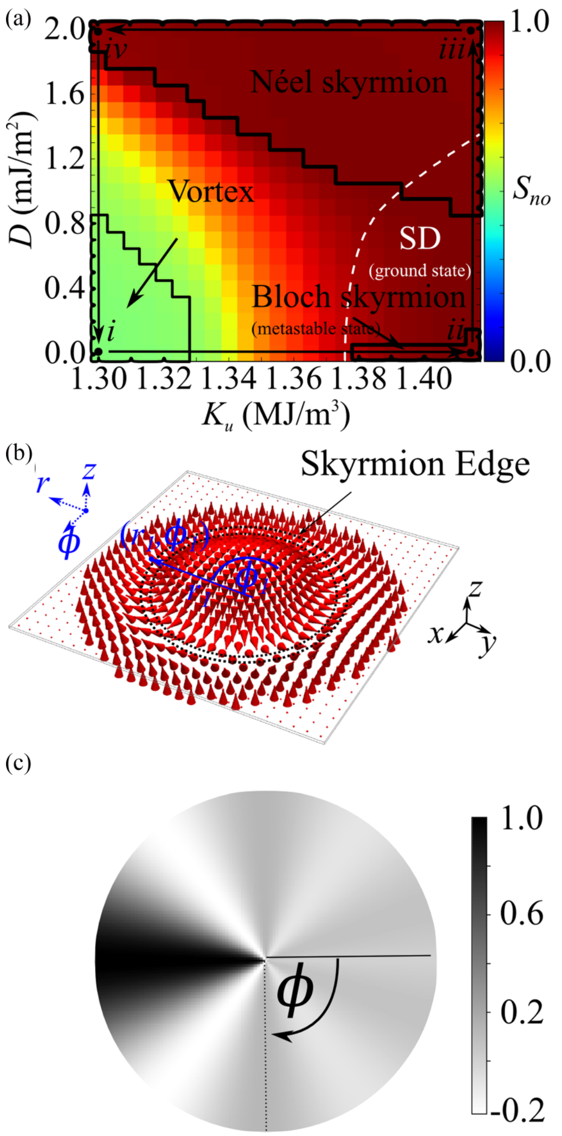

FIG. 1. (a) Skyrmion number S_{no} in a circular ferromagnetic dot as a function of magnetic anisotropy (K_{u}) and DMI strength, showing continuous transitions between four magnetization states (reprinted with permission from [46]. Copyright (2017) by the American Physical Society, https://doi.org/10.1103/PhysRevB.95.094414). (b) Néel skyrmion in a nanodot with a strong perpendicular magnetic anisotropy (large quality factor $Q = \frac{2K_{\text{u}}}{\mu_0 M_{\text{s}}^2}$). (c) Distribution of the amplitude of excitation magnetic field $\mathbf{B}_{\text{ext}} = I\,\text{sinc}(k_\phi(\phi - \pi))\text{sinc}(2\pi f_{\max} t)(1, 0, 1)$.

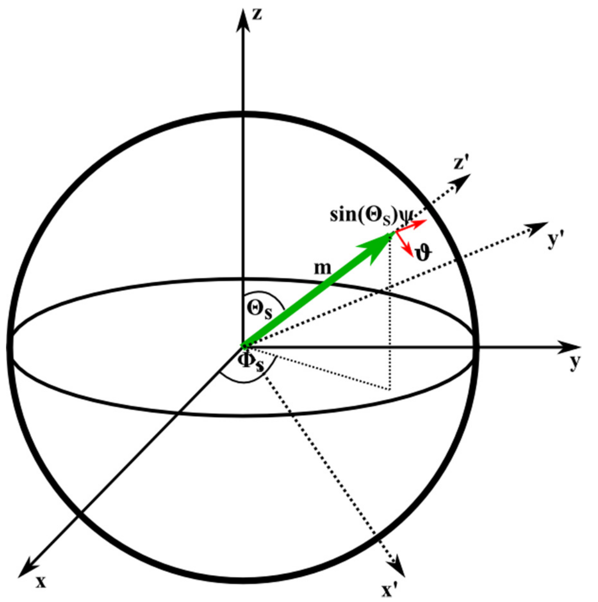

FIG. 2. Local coordinate frame with static magnetization vector (green) and dynamic magnetization components (red).

the cutoff frequency $f_{\max} = 10$ GHz and $t_0 = 1$ ns.[1] This value of the cutoff frequency was chosen because we were interested in mapping the low-frequency part of the SW excitation spectra related to different magnetization states of the dot.

For efficient excitation and detection of higher-order azimuthal modes (i.e., those with azimuthal mode index $|m| > 1$; see below for definition of m), a $\mathrm{sinc}(k_\phi(\phi - \pi))$ spatial modulation (dependence on the azimuthal angle ϕ, with $k_\phi = 2.5$) of the in-plane and out-of-plane driving magnetic fields was introduced in addition to the time modulation [see Fig. 1(c) for the field distribution in the circular dot]. Thus a number of azimuthal SWs with $|m| > 1$ could be efficiently coupled to the driving field. The inhomogeneous driving magnetic field with amplitude I used for the excitation had the following form:

$$\begin{aligned}\mathbf{B}_{\mathrm{ext}} = {}& [I\,\mathrm{sinc}(k_\phi(\phi - \pi))\mathrm{sinc}(2\pi f_{\max}(t - t_0)),0,\\ & \times I\,\mathrm{sinc}(k_\phi(\phi - \pi))\mathrm{sinc}(2\pi f_{\max}(t - t_0))]. \qquad (5)\end{aligned}$$

The space- and time-dependent magnetization components acquired after the field excitation were transformed to the frequency domain (Fourier transform[2]) to yield the power spectral density (PSD), SW eigenfrequencies, and spatial distribution of the dynamic components $\delta\mathbf{m}$ of selected eigenoscillations of the magnetization vector $\mathbf{m}$ [43].

We consider a linear SW dynamics over an inhomogeneous soliton magnetization background [54], $\Theta = \Theta_s + \vartheta$, $\Phi = \Phi_s + \psi$, where Θ_s and $\Phi_s = \Phi_0 + \phi$ are the spherical angles of the static skyrmion magnetization, and ϑ, ψ are the small SW angles ($\vartheta \ll 1$, $\psi \ll 1$), see Fig. 2. In the local coordinate frame with the Oz' axis directed along the skyrmion static magnetization $\mathbf{m}(\Theta_s,\Phi_s)$, the dynamic magnetization vector $\delta\mathbf{m}'$ is only determined by two components and can be represented as

$$\begin{aligned}\delta\mathbf{m}' &= [\vartheta, \sin(\Theta_s)\psi,0]\\ &= [a_n(r)\cos(m\phi - \omega t),b_n(r)\sin(m\phi - \omega t),0], \qquad (6)\end{aligned}$$

where a_n and b_n are the SW mode radial profiles, n is the number of nodes along the radial direction (radial mode index), m is the azimuthal mode index, and ϕ is the polar coordinate in the cylindrical system. The Cartesian magnetization components in the local coordinate frame $x'y'z'$ and the laboratory frame xyz are related by a rotation matrix $\mathcal{R}(\alpha,\beta,\gamma) = \exp(-i\alpha J_z)\exp(-i\beta J_y)\exp(-i\gamma J_z)$ (Chaps. 2 and 3 of Ref. [55]) parametrized by the Euler angles (α,β,γ): $\delta\mathbf{m} = \mathcal{R}(\Phi_s,\Theta_s,0)\delta\mathbf{m}'$ $(J = 1)$.

Below we consider azimuthal SW modes with the simplest radial coordinate dependence, described by $n = 0$, and a radially symmetric static magnetization configuration, $\Theta_s = \Theta_0(r)$ and $\Phi_0 = \Phi_0(r)$ [56]. The type of skyrmion (Bloch or Néel) is determined by the angle Φ_0 representing the skyrmion phase. It takes on values $\pm\frac{\pi}{2}$ for a magnetic vortex or complete Bloch skyrmion (the in-plane magnetization is aligned along the azimuthal direction throughout the dot, including the vortex/skyrmion edge) and $0,\pi$ for a complete Néel skyrmion (the in-plane component of the magnetization is along the radial direction).

The soliton dynamic magnetization components δm_r, δm_ϕ, δm_z in the laboratory frame (cylindrical coordinate system) [Fig. 1(b)] can be represented as a linear combination of the two magnetization components given by Eq. (6) involving the skyrmion static magnetization angles Θ_s and Φ_s. Accordingly, the azimuthal mode index m determines the number of nodes in the azimuthal angle ϕ dependencies of the magnetization components δm_r, δm_ϕ or δm_z. However, for the excitation of azimuthal SW modes, an in-plane variable magnetic field should be applied along the Ox or Oy in-plane directions. Therefore we rewrite the dynamic magnetization components in the laboratory coordinate frame xyz:

$$\begin{aligned}\delta m_x + i\delta m_y &= (\delta m_r + i\delta m_\phi)\exp(i\phi)\\ &= (\vartheta\cos(\Theta_s) + i\psi\sin(\Theta_s))\exp(i(\Phi_0 + \phi)),\\ \delta m_z &= -\sin(\Theta_s)\vartheta. \qquad (7)\end{aligned}$$

Let us assume that the skyrmion polarization $m_z(0) = p > 0$ and the static skyrmion profile $m_z(r) = \cos(\Theta_s(r))$ can be approximated by a step function, $\cos(\Theta_s(r)) = 1$ if $r < R_s$ and $\cos(\Theta_s(r)) = -1$ for $r > R_s$, i.e., the width of the radial domain wall delimiting the skyrmion is small in comparison with the skyrmion radius R_s, defined by the equation $m_z(R_s) = 0$. Then, for the Cartesian magnetization components $\delta m_x,\delta m_y$, the azimuthal mode index m is shifted to $m + 1$ within the skyrmion, $r < R_s$, and to $m - 1$ beyond it, $r > R_s$. The shift of the index m is opposite for $p < 0$. The shift can be obtained from Eq. (7) by the substitution of the dynamic magnetization components $\vartheta, \psi\sin(\Theta_s)$ given by Eq. (6).

Throughout the present paper we use the following values of material parameters of the considered ultrathin magnetic circu-

---

[1] We used a cell size below 1 nm, $\frac{250\times10^{-9}}{256}$. The maximum amplitude of the sinc signal was $I = 0.5$ mT.

[2] The rectangular window function was used in the Fourier transform with 50 ns width, starting 4 ns after the peak of the sinc signal, with a frequency resolution $\Delta f = 20$ MHz.

lar dot of radius $R = 125$ nm and thickness $t = 1.4$ nm: saturation magnetization $M_s = 1.5 \times 10^6$ A/m, exchange stiffness constant $A = 3.1 \times 10^{-11}$ J/m, DMI constant D ranging from 0 to 3.8×10^{-3} J/m^2, and out-of-plane magnetic anisotropy constant K_u ranging from 1.30×10^6 to 1.415×10^6 J/m^3. This set of parameter values corresponds to CoFeB-MgO ultrathin films [57]. The assumed material quality factor $Q = \frac{2K_u}{\mu_0 M_s^2}$ ranges from 0.92 to 1.0. The Gilbert damping parameter used in the FDTD simulations is $\alpha = 0.01$, a value close to that of a CoFeB ultrathin film [58,59]. The present study is also extended to higher interface DMI values, bulk DMI, and different dot sizes.

III. RESULTS AND DISCUSSION

Figure 1(a) shows a color map representing the skyrmion number versus the DMI strength and uniaxial anisotropy constant. In this color map, we can choose paths, indicated by black straight arrows, corresponding to continuous transitions between different soliton equilibrium configurations: (i) → (ii) between a vortex and a Bloch skyrmion, (ii) → (iii) between the Bloch skyrmion and a high-Q Néel skyrmion, (iii) → (iv) between the high-Q Néel skyrmion and a low-Q Néel skyrmion, and, finally, (iv) → (i) between the low-Q Néel skyrmion and the vortex. Figure 1(b) shows a high-Q Néel skyrmion. The indicated ring, in which the z-component of magnetization is approximately zero ($m_z \approx 0$), represents the skyrmion edge. The magnetization states corresponding to points (i) to (iv) are presented in Ref. [46].

Figure 3(a) shows the calculated frequencies of low-frequency spin excitations along the paths specified above. The number of observed SW modes is larger than that of modes excited by a uniform magnetic field, discussed in Ref. [46]. In Figs. 3(b)–3(e), characteristic parameters of the static skyrmions are plotted versus magnetic parameters of the dot. Clearly discernible regions corresponding to complete vortex, Bloch skyrmion, Néel skyrmion, and intermediate magnetization configurations are indicated in Figs. 3(b), 3(c) and 1(a). Figure 3(e) demonstrates second-order phase transitions, i.e., continuous transitions of the magnetization components $\langle m_z \rangle$, $\langle m_r \rangle$, and $\langle m_\phi \rangle$ averaged over the dot volume along the paths. Full spin excitation spectra are considered with the magnetic parameters changing along the paths (i)→(ii)→(iii)→(iv) to enable a complete comparison with the spectra calculated in Ref. [46]. However, we discuss mostly the left half of the spectrum with increasing anisotropy and DMI [path (i)→(ii)→(iii)].

In the dynamic simulations, we find spin eigenmodes maintaining the radial symmetry of the soliton static state (radially symmetric or breathing modes with $m = 0$) as well as eigenmodes with broken radial symmetry [clockwise (CW) and counter-clockwise (CCW) rotating azimuthal modes]. The radially symmetric modes have no net in-plane magnetization, and therefore can only be excited by an out-of-plane variable magnetic field [43]. The azimuthal modes with $|m| = 1$, including the gyrotropic mode, can be excited by a uniform in-plane variable magnetic field, whereas the SW modes with higher azimuthal indexes ($|m| > 1$) cannot be excited by a uniform field due to the symmetry of their microwave magnetization distribution. A nonuniform excitation field as described in Sec. II was used for the excitation of higher-order azimuthal SW modes.

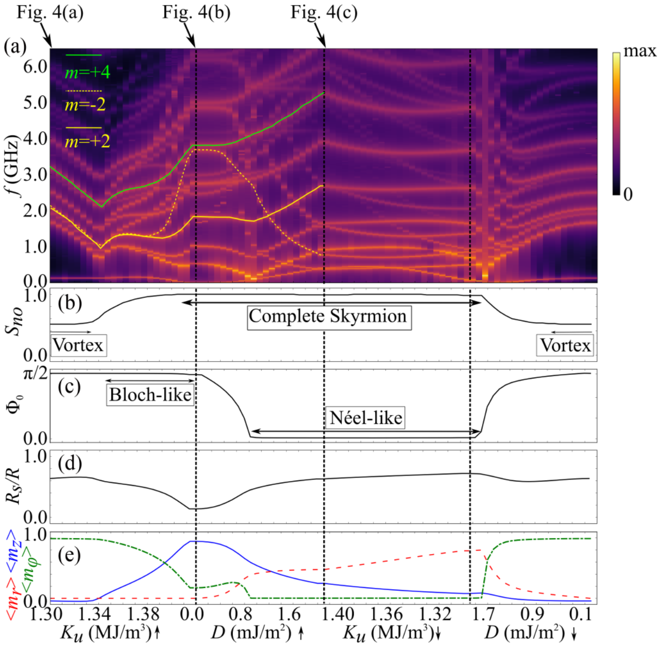

FIG. 3. (a) Frequencies of spin waves excited by a nonuniform magnetic field plotted along the paths, indicated in Fig. 1(a), between four inhomogeneous magnetization configurations (i)–(iv). Below, static properties of respective solitons: (b) skyrmion number $S_{\rm no}$, (c) average skyrmion phase Φ_0, (d) reduced skyrmion radius R_s/R, and (e) average magnetization components $\langle m_r \rangle$, $\langle m_\phi \rangle$ and $\langle m_z \rangle$, plotted as red dashed, green dot-dashed and blue continuous lines, respectively.

Figure 3(a) shows a continuous frequency evolution of the azimuthal SW modes. All the azimuthal SW excitations over the vortex background have their counterparts in the skyrmion states. The first striking observation is the lifting of the frequency degeneracy of the SW modes with $m = \pm|m|$, $|m| > 1$. In the vortex states, these modes are almost completely degenerate (their frequency splitting is negligible), and the degeneracy is determined by the azimuthal number m; see Fig. 4(a) for the distribution of the amplitude and phase of the z-component δm_z of dynamic magnetization. In the mixed states and the Néel and Bloch skyrmion states, this degeneracy is lifted [see modes $m = +2$ and -2 in Fig. 3(a), represented by solid yellow and dashed yellow lines, respectively, above $K_u = 1.38 \times 10^6$ J/m^3]. However, another degeneracy (change in the systematics of eigenfrequencies) is observed in the Bloch skyrmion [see Fig. 3(a), modes with $m = +4$ and -2, represented by solid green and dashed yellow lines, respectively, at $K_u = 1.415 \times 10^6$ J/m^3].

The lifting of mode degeneracy in the mixed states and the different pairing of azimuthal modes in the vortex/Bloch skyrmion states are due to the different magnetic configurations and regions of strongest localization of the SW amplitude in these states. In a vortex, azimuthal SWs with $|m| > 1$ are localized near the edge of the dot, where in-plane magnetization dominates and curls around the center of the dot with cylindrical symmetry. As the anisotropy increases, a static vortex evolves into a Bloch skyrmion; the out-of-plane magnetization component gradually increases. However, due

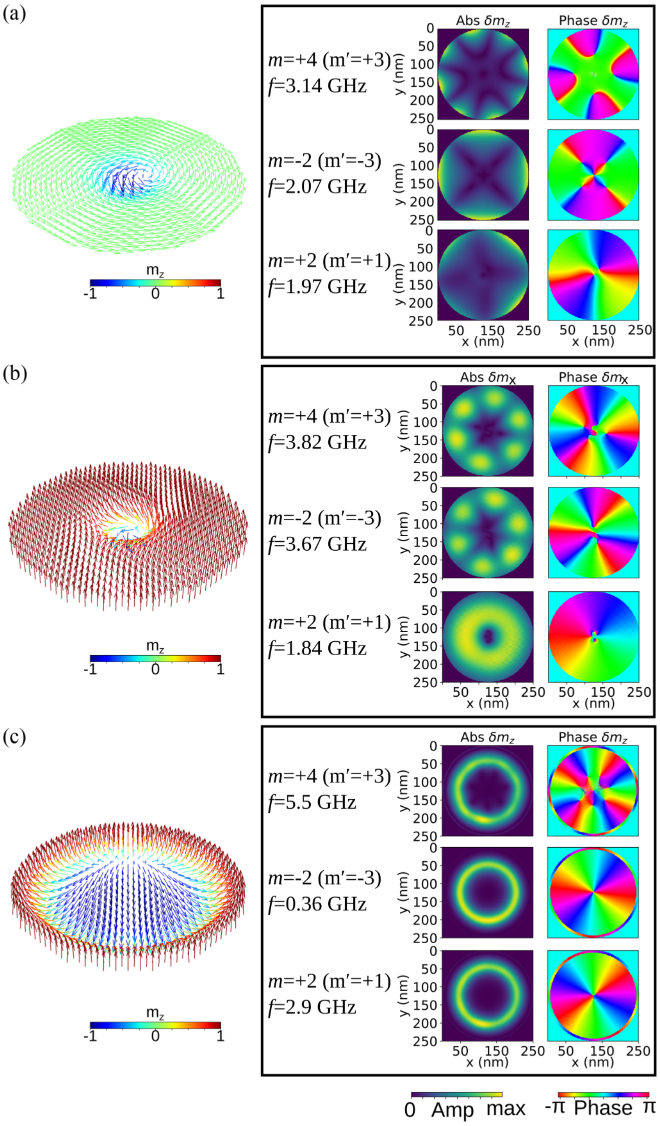

FIG. 4. Spatial distribution of the static magnetization (left column) and SW eigenmodes (right column) (amplitude and phase of the x or z dynamic magnetization component) for three different modes with azimuthal mode indices $m = +4, -2$ and $+2$. In brackets, the number of nodes in the dynamic magnetization components m_x and m_y. The magnetic parameters are (a) $K_\mathrm{u} = 1.30$ MJ/m^3, $D = 0$, vortex (i); (b) $K_\mathrm{u} = 1.415$ MJ/m^3, $D = 0$, Bloch skyrmion (ii), and (c) $K_\mathrm{u} = 1.415$ MJ/m^3, $D = 2.0$ mJ/m^2, Néel skyrmion (iii).

to the small size of the skyrmion, SWs are still localized at the edge of the dot, where the static magnetization is perpendicular to the dot plane [see Fig. 4(b) for the distribution of the amplitude and phase of the x-component δm_x of the dynamic magnetization]. The number of azimuthal nodes of the degenerate SW modes in the Bloch-skyrmion states differs by ±1, according to the mode numbering scheme presented in Sec. II.

A continuous transition from vortex to Bloch skyrmion occurs with gradually increasing anisotropy constant K_u. An SW mode localized in the area of cylindrically symmetric in-plane magnetization becomes localized in the area of out-of-plane magnetization. In this sense, the magnetization state supporting azimuthal SWs in the vortex to Bloch skyrmion transition is similar to that in a thin ring, presented in Fig. 5 in Ref. [51]. In the cited study, the magnetic configuration in the ring is changed from a vortex state to a uniform out-of-plane state by applying an external out-of-plane magnetic field. When the applied field is zero, the vortex state is stable and azimuthal modes with $\pm m$ are degenerated. As the out-of-plane field increases, the vortex evolves continuously into an SD state with an out-of-plane configuration. Unlike in the ring, however, in the soliton state dot the low frequency modes with $m = 0$ (breathing) and $m = -1$ (gyrotropic) are not degenerate due to their coupling to the soliton motion.[3]

In the ring, the degeneracy lifting in intermediate states and the different systematics of SW modes in the vortex and out-of-plane magnetization states are attributed to the geometrical Berry phase, which occurs in the vortex state and vanishes in the out-of-plane state [51]. The same explains the degeneracy lifting and the change in the systematics of SW frequencies in our investigation. Taking account of the z component of the gauge vector potential [54] (resulting in the topological Berry phase) increases the azimuthal SW mode index from m to $m' = m - 1$ in a saturated out-of-plane state and leads to the degeneracy of edge-localized modes with azimuthal mode index $\pm m'$ in the Bloch skyrmion state. This explains, for instance, the lifting of the degeneracy of the $m = \pm 2$ modes with increasing K_u and the appearance of degeneracy of the azimuthal modes with $m = +4$, $m' = +3$ and $m = -2$, $m' = -3$ in the Bloch skyrmion state [see Figs. 2 and 3(b)]. The latter degeneracy disappears in the course of the transition from the Bloch skyrmion to Néel skyrmion configuration with increasing DMI strength D.

Next, we studied the influence of the DMI strength on azimuthal SW modes. With increasing DMI constant [path (ii) → (iii) in Fig. 1(a)] the CW and CCW azimuthal modes diverge, their frequencies split. Figure 5 shows the azimuthal mode frequencies plotted versus the DMI strength in the range $D = 0$-3.8×10^{-3} J/m^2. A pronounced splitting of the CW ($m < 0$) and CCW ($m > 0$) azimuthal modes is observed for strong DMI.

The frequency splitting results from two factors. Firstly, we note that the size of the skyrmion increases with DMI strength. The DMI introduces conditions that favor localization of azimuthal SW modes at the edge of the skyrmion; see the amplitude localization of the z-component δm_z of dynamic magnetization in Fig. 4(c). The edge of the skyrmion acts as a channel for SW propagation, playing a role similar to that of domain walls in planar nanostructures [60]. The static magnetization components are cylindrically symmetric at the edge of the skyrmion. As observed above, the frequency degeneracy is determined by the number of nodes in the δm_r and δm_ϕ components of the dynamic magnetization. This might affect the SW spectrum in the range of weak DMI and saturate the frequency splitting when localization at the skyrmion edge is fully realized. The other factor that might contribute to

---

[3] In independent simulations, we observed degeneracy lifting in intermediate magnetic states and different pairing of modes in a vortex/SD out-of-plane configuration in a ring.

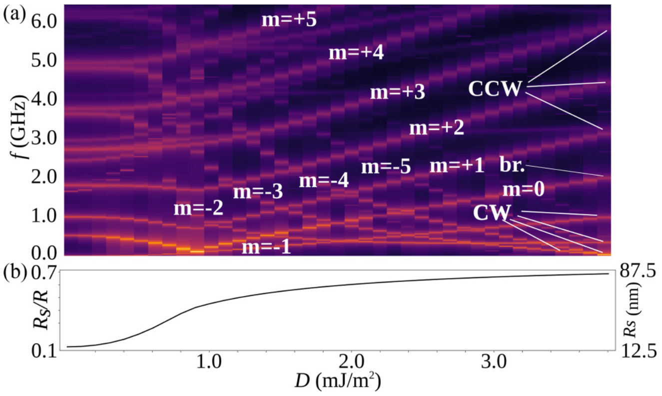

FIG. 5. (a) Frequency spectrum of azimuthal SW modes vs the DMI constant D, ranging from 0 to 3.8×10^{-3} J/m^2, with the out-of-plane magnetic anisotropy constant fixed at $K_u = 1.415\times10^6$ J/m^3. Pronounced frequency splitting of CW and CCW azimuthal modes is observed for high D values. (b) Skyrmion size vs D.

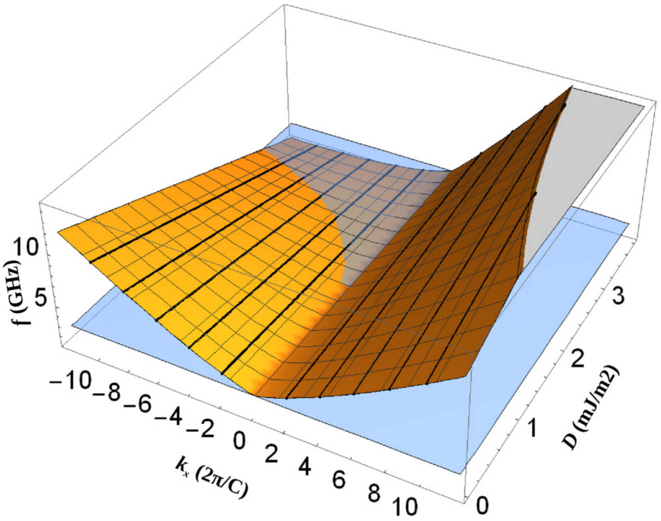

FIG. 6. Dispersion relation of spin waves propagating in a thin film in a direction perpendicular to the in-plane magnetization. Negative group velocity and strong nonreciprocity are observed at high values of the DMI constant D. Black lines represent wave vectors corresponding to azimuthal spin waves localized near the edge of a skyrmion with radius $R_s = 75$ nm. Several SW modes are predicted to have a frequency lower than the $m = 0$ radial mode frequency $f_0(k = 0)$, represented by the transparent blue plane.

the frequency splitting of azimuthal SW modes is the DMI-induced SW nonreciprocity [8]. Spin-wave propagation is nonreciprocal when perpendicular to the in-plane magnetic field. This condition is fulfilled by the azimuthal SWs localized at the skyrmion edge, and nonreciprocity can have an effect on their spectrum.

Nonreciprocal dispersion of SWs in an infinite film uniformly magnetized in the film plane accounting an interface DMI is illustrated by the 3D plot presented in Fig. 6. Although this model cannot be used for the estimation of SW frequencies in a vortex/skyrmion state dot, it does, however, allow us to predict qualitatively effects resulting from nonreciprocal SW propagation. The graph is based on the analytical formula for SW frequency in an infinite film in the Damon-Eschbach geometry [61–63]:

$$f = \frac{1}{2\pi}\sqrt{(\gamma B_0 + \omega_{\mathrm{ex}}k^2)(\gamma B_0 + \omega_{\mathrm{ex}}k^2 + \omega_{\mathrm{M}}) + \frac{\omega_M^2}{4}(1 - e^{-2|k|t})} + \frac{\gamma Dk}{\pi M_{\mathrm{s}}}, \tag{8}$$

where $\omega_{\mathrm{M}} = \gamma\mu_0 M_{\mathrm{s}}$, $\omega_{\mathrm{ex}} = \frac{2\gamma A}{M_{\mathrm{s}}}$, B_0 is the external static magnetic field, k the is in-plane wave vector, and t is the film thickness. The magnetic anisotropy is neglected. The DMI introduces the linear term proportional to the wave vector, which splits the energy of SWs propagating in opposite directions.

The following parameters were used to approximate the conditions of SW propagation at the edge of the skyrmion: $M_{\mathrm{eff}} = 0.8$ MA/m [64], $B_0 = 0.1$ T, and $C = 2\pi R_s$, corresponding to the circumference of the skyrmion with $R_{\mathrm{s}}/R = 0.6$. The black lines in the plot in Fig. 6 represent the wave vectors $k_m = m/R_s$, which can be assigned to azimuthal modes with different m (the wavelength is $\lambda = C/m$); the blue plane indicates the frequency $f_0 = f(k = 0)$ of the $m = 0$ mode. Several m modes with $k < 0$ are found to intersect with the $|m| = 0$ mode in the DMI range from 0 to 3 mJ/m^2. At high D values, close to 3 mJ/m^2, the SW group velocity is negative for several quantizations, which suggests that the frequency might decrease with quantization of $m < 0$ azimuthal SWs in the skyrmion state. Indeed, such an effect is observed in the dot; in Fig. 5, azimuthal SW mode frequencies cross above $D = 2.0$ mJ/m^2. The increase in the frequencies of $m > 0$ modes can be related to the increase of the frequency of SWs propagating in $k > 0$ direction.

The inversion of CW spin-wave modes (frequency decrease with increasing azimuthal mode index $|m|$) becomes more pronounced with increasing skyrmion radius, because of the decreasing distance between the allowed wave vectors of these SWs. Figure 7 shows the SW frequency spectrum versus the dot radius R, ranging from 30 to 180 nm, for $D = 3$ mJ/m^2. With increasing dot radius also the skyrmion increases in size. Frequency inversion is only possible when the skyrmion size is sufficiently large. Note the different behavior of the $m = 0$ and $m = -1$ modes, associated with breathing and gyrotropic motion of the skyrmion, respectively. Due to its coupling to the soliton motion the breathing mode has a low frequency even in a small-sized skyrmion. The frequency of the gyrotropic mode approaches zero near the instability limit of the skyrmion magnetization configuration. This is yet another confirmation of the different character of excitation modes with $m = -1$ and $m = +1$ discussed in Ref. [46].

Above we demonstrated the nonreciprocity of SW propagation induced by interfacial DMI in the Néel skyrmion

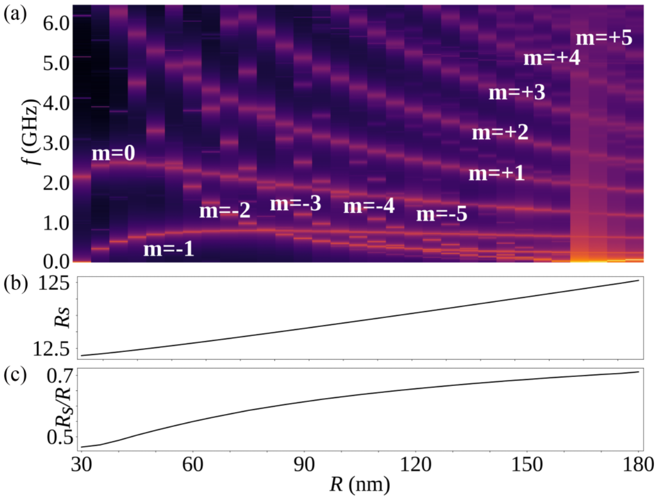

FIG. 7. (a) Spectrum of azimuthal spin waves vs the radius R of the dot with the DMI strength fixed at $D = 3 \times 10^{-3}$ J/m^2. The CW propagating spin waves show a considerable frequency decrease with increasing R. Coupling of the $m = 0$ (breathing) and $m = -1$ (gyrotropic) modes to the soliton motion is evidenced by their low frequency even in a small-sized skyrmion. (b) Skyrmion radius and (c) normalized skyrmion radius vs the dot radius.

state. Bulk DMI stabilizing a Bloch skyrmion results in SW frequency nonreciprocity when the wave propagation direction is parallel to the in-plane magnetization [10]. Since this condition for nonreciprocal SW propagation is satisfied on the edge of such a Bloch skyrmion, effects similar to those described above are expected for bulk DMI as well. Although nonzero values of the bulk DMI constant D_{bulk} are not expected in the studied ultrathin dots, it is instructive to calculate the influence of bulk DMI on the SW spectrum. Figure 8 shows the SW frequency spectrum as a function of the bulk DMI strength D_{bulk}. A frequency splitting qualitatively the same as in a Néel skyrmion with interfacial DMI (Fig. 5) is observed in the spectrum of SW modes excited in the Bloch skyrmion state.

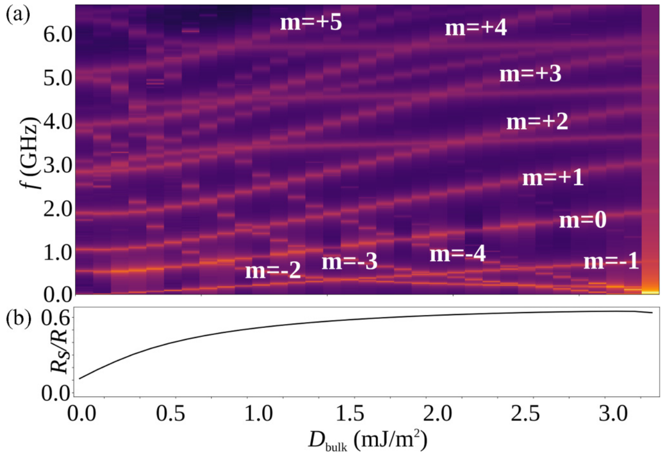

FIG. 8. (a) Spectrum of azimuthal SW modes vs the bulk DMI constant D_{bulk} at $K_{\text{u}} = 1.415 \times 10^6$ J/m^3. A pronounced splitting of CW and CCW azimuthal modes is observed at high values of D_{bulk}. (b) Skyrmion size vs D_{bulk}.

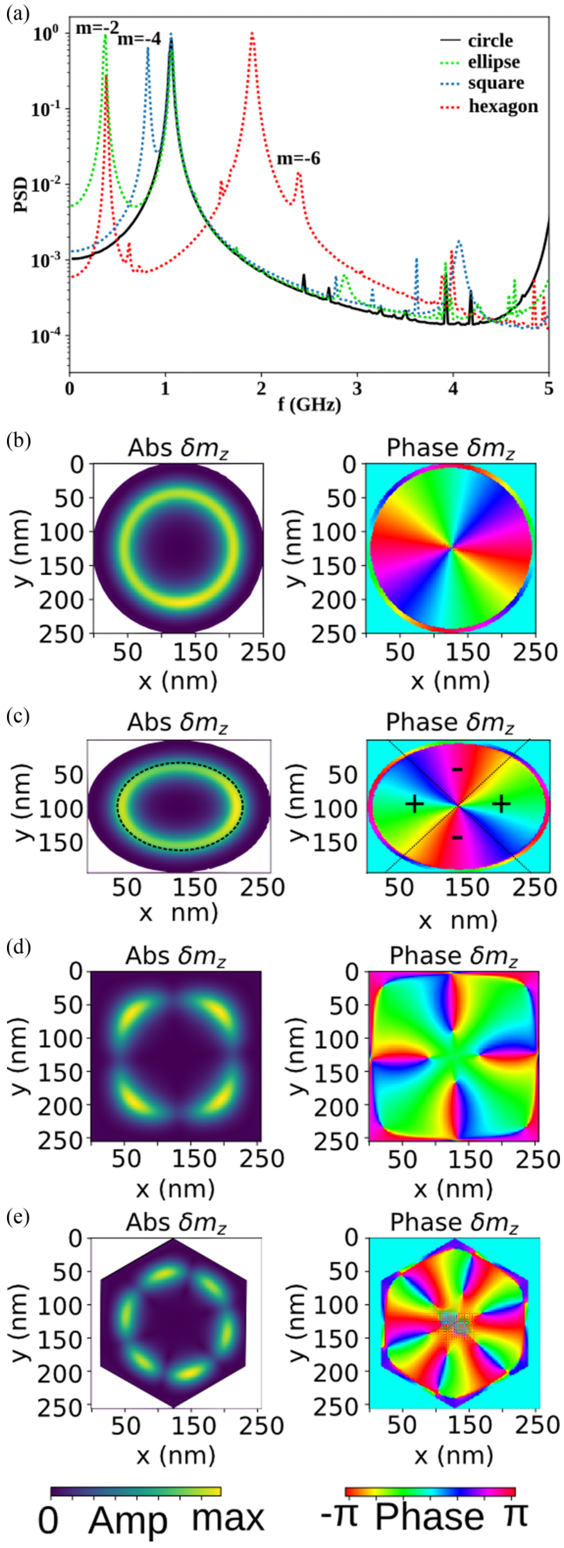

FIG. 9. (a) PSD spectrum of circular, elliptical, square, and hexagonal nanoelements. (b)–(e) Distribution of the z component of the dynamic magnetization of the mode corresponding to the symmetry of the nanoelement in the shape of a circle (radius $R = 125$ nm), square (side length $= 250$ nm), ellipse (major semiaxis $a = 135$ nm, minor semiaxis $b = 115$ nm), and hexagon (side length $l = 125$ nm), respectively.

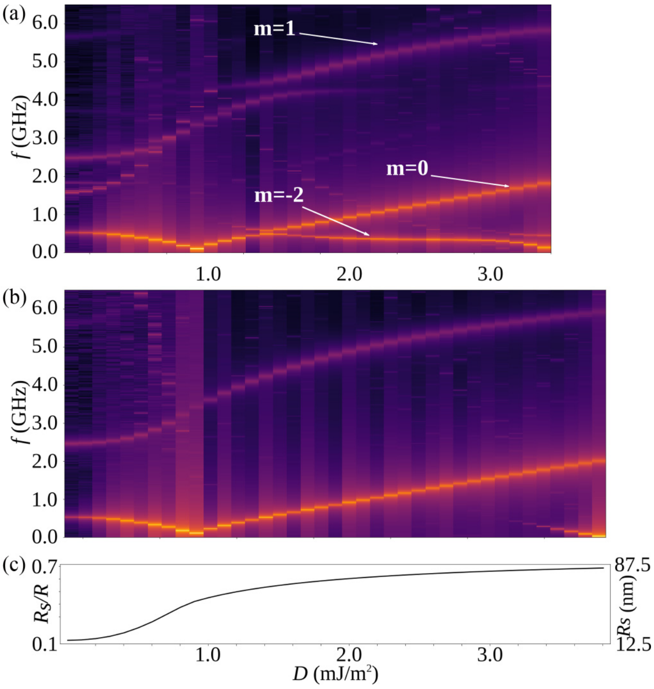

FIG. 10. (a) Spectrum of spin waves excited by a uniform out-of-plane microwave field in an elliptical nanodot ($a = 135$ nm, $b = 115$ nm). (b) Spectrum of spin waves excited by a uniform out-of-plane microwave field in a circular nanodot ($R = 125$ nm). (c) Skyrmion size vs the interface DMI strength D for the circular dot.

This result can help understand the frequencies of azimuthal SWs observed in Bloch skyrmion dots stabilized by D_{bulk} [44].

Finally, we have studied the influence of the shape of the dot on the efficiency of coupling of azimuthal SWs to a uniform microwave magnetic field. Since the shape of the nanodot affects the skyrmion edge, deformation is expected to have an effect on the coupling, too. As shown in Fig. 9, for $D = 2.2$ mJ/m^2 ($D = 3.4$ mJ/m^2 in the case of hexagon for a lower frequency of the $m = -6$ mode) the amplitude of the $m = -2$ mode is localized at the edge of the elliptical skyrmion (indicated by black dashed line). A change in the proportion of areas of in-phase and antiphase oscillations in the dot results in an increased coupling of the dynamic magnetization to a spatially uniform external magnetic field. Moreover, an increased amplitude intensity is observed close to the major semiaxis of the ellipse. This does not occur for the $m = +2$ mode, in which case the coupling increases only slightly with respect to that in the circular nanodot. We also observe a negligible change in frequency of the $m = 0$ breathing mode as a result of changing the dot shape from circular to elliptical.

Also in nanodots with other symmetries, such as a square or a hexagon, the coupling of the dynamic magnetization to a uniform in-plane magnetic field can be relatively strong. One can conclude that the efficiency of the coupling of a SW mode with the azimuthal index corresponding to the order of rotational symmetry decreases with increasing symmetry of the dot.

In Fig. 10, we compare the DMI-strength dependence of the SW spectrum of circular and elliptical nanodots. For small values of D, the azimuthal SW modes are localized outside of the skyrmion. The $m = -2$ mode is not coupled to a uniform out-of-plane field. Around $D = 1$ mJ/m^2 the skyrmion radius increases, the mode localization area shifts to the skyrmion edge, and a uniform out-of-plane magnetic field efficiently excites the $m = -2$ mode. Additionally, hybridization between the radially quantized mode and azimuthal SWs is induced by the elliptical symmetry.

IV. SUMMARY

We have calculated the spectra of high-order azimuthal spin waves in planar nanoelements. The azimuthal SWs found in a circular dot in the vortex state are mapped into azimuthal SWs in the Bloch and Néel skyrmion states. The nanodot edge localization found in the vortex state is also observed in small-sized skyrmions; however, the frequency degeneracy of the modes is different in the skyrmion states. The observed difference in the systematics of frequency levels is due to the geometrical Berry phase, which occurs for the dot edge-localized SWs in the vortex state, but not in the small skyrmion state.

Large-sized skyrmions provide a possibility of SW channeling at the skyrmion edge. Skyrmion edge localization and the DMI account for the relatively strong nonreciprocity of azimuthal SWs. The frequency difference between azimuthal spin waves propagating in opposite directions is substantial, and there is a significant frequency splitting between CW and CCW modes. The effect is compared to the DMI-induced frequency splitting of spin waves propagating in an infinite thin film. Moreover, efficient coupling of azimuthally symmetric spin-wave modes with azimuthal index $|m| > 1$ to an external uniform microwave magnetic field is observed in dots of non-circular symmetry in the skyrmion state. The obtained results help understand the skyrmion dynamics in ultrathin nanodots of different shapes, provide a route to manipulate skyrmions in patterned nanostructures, and indicate a method for experimental measurement of azimuthal spin waves. The understanding of single-skyrmion spin excitations should also be of help in the analysis of the magnetization dynamics in skyrmion lattices.

ACKNOWLEDGMENTS

This study is part of a project financed by the SASPRO Programme. The research received funding from the People Programme (Marie Curie Actions) of the European Union's Seventh Framework Programme under REA Grant Agreement No. 609427 (project WEST 1244/02/01) and was further co-funded by the Slovak Academy of Sciences and the European Union Horizon 2020 Research and Innovation Programme under Marie Sklodowska-Curie Grant Agreement No. 644348 (MagIC). We acknowledge financial support from the Slovak Grant Agency APVV (Grant No. APVV-16-0068, NanoSky) and the Slovak Scientific Grant Agency VEGA (Project No. 2/0183/15). K.G. acknowledges support by IKERBASQUE (the Basque Foundation for Science) and the Ministerio de Economía y Competitividad de España Grant No. FIS2016-78591-C3-3-R.

[1] C.-P. Chui, Y. Zhou, and W. Liu, Technology **19**, 18 (2017).
[2] R. Tomasello, E. Martinez, R. Zivieri, L. Torres, M. Carpentieri, and G. Finocchio, Sci. Rep. **4**, 6784 (2014).
[3] A. Khitun, J. Appl. Phys. **111**, 054307 (2012).
[4] O. Boulle, J. Vogel, H. Yang, S. Pizzini, D. de Souza Chaves, A. Locatelli, T. O. Menteş, A. Sala, L. D. Buda-Prejbeanu, O. Klein *et al.*, Nat. Nanotechnol. **11**, 449 (2016).
[5] C. Moreau-Luchaire, C. Moutafis, N. Reyren, J. Sampaio, C. Vaz, N. Van Horne, K. Bouzehouane, K. Garcia, C. Deranlot, P. Warnicke *et al.*, Nat. Nanotechnol. **11**, 444 (2016).
[6] F. Garcia-Sanchez, P. Borys, A. Vansteenkiste, J.-V. Kim, and R. L. Stamps, Phys. Rev. B **89**, 224408 (2014).
[7] A. Fert, V. Cros, and J. Sampaio, Nat. Nanotechnol. **8**, 152 (2013).
[8] L. Udvardi and L. Szunyogh, Phys. Rev. Lett. **102**, 207204 (2009).
[9] J.-H. Moon, S.-M. Seo, K.-J. Lee, K.-W. Kim, J. Ryu, H.-W. Lee, R. D. McMichael, and M. D. Stiles, Phys. Rev. B **88**, 184404 (2013).
[10] D. Cortés-Ortuño and P. Landeros, J. Phys.: Condens. Matter **25**, 156001 (2013).
[11] M. Mruczkiewicz and M. Krawczyk, Phys. Rev. B **94**, 024434 (2016).
[12] A. Hrabec, M. Belmeguenai, A. Stashkevich, S. Chérif, S. Rohart, Y. Roussigné, and A. Thiaville, Appl. Phys. Lett. **110**, 242402 (2017).
[13] K. Y. Guslienko, S. O. Demokritov, B. Hillebrands, and A. N. Slavin, Phys. Rev. B **66**, 132402 (2002).
[14] C. Bayer, S. Demokritov, B. Hillebrands, and A. Slavin, Appl. Phys. Lett. **82**, 607 (2003).
[15] L. Giovannini, F. Montoncello, F. Nizzoli, G. Gubbiotti, G. Carlotti, T. Okuno, T. Shinjo, and M. Grimsditch, Phys. Rev. B **70**, 172404 (2004).
[16] M. Buess, R. Höllinger, T. Haug, K. Perzlmaier, U. Krey, D. Pescia, M. R. Scheinfein, D. Weiss, and C. H. Back, Phys. Rev. Lett. **93**, 077207 (2004).
[17] J. P. Park and P. A. Crowell, Phys. Rev. Lett. **95**, 167201 (2005).
[18] M. Buess, T. P. J. Knowles, R. Höllinger, T. Haug, U. Krey, D. Weiss, D. Pescia, M. R. Scheinfein, and C. H. Back, Phys. Rev. B **71**, 104415 (2005).
[19] X. Zhu, Z. Liu, V. Metlushko, P. Grütter, and M. R. Freeman, Phys. Rev. B **71**, 180408 (2005).
[20] R. Zivieri and F. Nizzoli, Phys. Rev. B **71**, 014411 (2005).
[21] C. E. Zaspel, B. A. Ivanov, J. P. Park, and P. A. Crowell, Phys. Rev. B **72**, 024427 (2005).
[22] S. Mamica, Acta Phys. Pol. A **127**, 365 (2015).
[23] P. Lupo, D. Kumar, and A. Adeyeye, AIP Adv. **5**, 077179 (2015).
[24] G. N. Kakazei, P. Wigen, K. Y. Guslienko, V. Novosad, A. Slavin, V. Golub, N. Lesnik, and Y. Otani, Appl. Phys. Lett. **85**, 443 (2004).
[25] A. A. Awad, K. Guslienko, J. Sierra, G. N. Kakazei, V. Metlushko, and F. Aliev, Appl. Phys. Lett. **96**, 012503 (2010).
[26] G. Gubbiotti, G. Carlotti, T. Okuno, M. Grimsditch, L. Giovannini, F. Montoncello, and F. Nizzoli, Phys. Rev. B **72**, 184419 (2005).
[27] V. E. Demidov, M. Buchmeier, K. Rott, P. Krzysteczko, J. Münchenberger, G. Reiss, and S. O. Demokritov, Phys. Rev. Lett. **104**, 217203 (2010).
[28] H. T. Nembach, J. M. Shaw, T. J. Silva, W. L. Johnson, S. A. Kim, R. D. McMichael, and P. Kabos, Phys. Rev. B **83**, 094427 (2011).
[29] J. Podbielski, F. Giesen, and D. Grundler, Phys. Rev. Lett. **96**, 167207 (2006).
[30] I. Neudecker, M. Kläui, K. Perzlmaier, D. Backes, L. J. Heyderman, C. A. F. Vaz, J. A. C. Bland, U. Rüdiger, and C. H. Back, Phys. Rev. Lett. **96**, 057207 (2006).
[31] G. Gubbiotti, M. Madami, S. Tacchi, G. Carlotti, H. Tanigawa, T. Ono, L. Giovannini, F. Montoncello, and F. Nizzoli, Phys. Rev. Lett. **97**, 247203 (2006).
[32] F. Giesen, J. Podbielski, and D. Grundler, Phys. Rev. B **76**, 014431 (2007).
[33] H. Schultheiss, S. Schäfer, P. Candeloro, B. Leven, B. Hillebrands, and A. N. Slavin, Phys. Rev. Lett. **100**, 047204 (2008).
[34] S. Mamica, J. Appl. Phys. **114**, 233906 (2013).
[35] S. Mamica, Low Temp. Phys. **41**, 806 (2015).
[36] J. A. Otálora, M. Yan, H. Schultheiss, R. Hertel, and A. Kákay, Phys. Rev. B **95**, 184415 (2017).
[37] M. D. DeJong and K. L. Livesey, Phys. Rev. B **95**, 054424 (2017).
[38] K. Wagner, A. Kákay, K. Schultheiss, A. Henschke, T. Sebastian, and H. Schultheiss, Nat. Nanotech. **11**, 432 (2016).
[39] A. Lara, J. R. Moreno, K. Y. Guslienko, and F. G. Aliev, Sci. Rep. **7**, 5597 (2017).
[40] F. Garcia-Sanchez, P. Borys, R. Soucaille, J.-P. Adam, R. L. Stamps, and J.-V. Kim, Phys. Rev. Lett. **114**, 247206 (2015).
[41] J.-V. Kim, F. Garcia-Sanchez, J. Sampaio, C. Moreau-Luchaire, V. Cros, and A. Fert, Phys. Rev. B **90**, 064410 (2014).
[42] Z. V. Gareeva and K. Y. Guslienko, Phys. Status Solidi (RRL) - Rapid Res. Lett. **10**, 227 (2016).
[43] M. Mruczkiewicz, P. Gruszecki, M. Zelent, and M. Krawczyk, Phys. Rev. B **93**, 174429 (2016).
[44] M. Beg, M. Albert, M.-A. Bisotti, D. Cortés-Ortuño, W. Wang, R. Carey, M. Vousden, O. Hovorka, C. Ciccarelli, C. S. Spencer *et al.*, Phys. Rev. B **95**, 014433 (2017).
[45] K. Y. Guslienko and Z. V. Gareeva, IEEE Magnet. Lett. **8**, 4100305 (2017).
[46] M. Mruczkiewicz, M. Krawczyk, and K. Y. Guslienko, Phys. Rev. B **95**, 094414 (2017).
[47] Y. Liu, R. K. Lake, and J. Zang, J. Magn. Magn. Mater. (2017), doi:10.1016/j.jmmm.2017.07.007.
[48] Z.-x. Li, Y.-f. Chen, Z.-w. Zhou, Y.-z. Nie, Q.-l. Xia, D.-w. Wang, and G.-h. Guo, J. Magn. Magn. Mater. **433**, 216 (2017).
[49] M. Garst, J. Waizner, and D. Grundler, J. Phys. D **50**, 293002 (2017).
[50] J. Kim, J. Yang, Y.-J. Cho, B. Kim, and S.-K. Kim, Sci. Rep. **7**, 45185 (2017).
[51] V. K. Dugaev, P. Bruno, B. Canals, and C. Lacroix, Phys. Rev. B **72**, 024456 (2005).
[52] A. Vansteenkiste, J. Leliaert, M. Dvornik, M. Helsen, F. Garcia-Sanchez, and B. Van Waeyenberge, AIP Adv. **4**, 107133 (2014).
[53] A. N. Bogdanov and U. K. Rößler, Phys. Rev. Lett. **87**, 037203 (2001).
[54] K. Guslienko, EPL **113**, 67002 (2016).
[55] A. R. Edmonds, *Angular Momentum in Quantum Mechanics* (Princeton University Press, Princeton, 2016), Chaps. 2 and 3.
[56] K. Y. Guslienko, IEEE Magn. Lett. **6**, 4000104 (2015).
[57] Y. Nakatani, M. Hayashi, S. Kanai, S. Fukami, and H. Ohno, Appl. Phys. Lett. **108**, 152403 (2016).

[58] A. Natarajarathinam, Z. R. Tadisina, T. Mewes, S. Watts, E. Chen, and S. Gupta, J. Appl. Phys. **112**, 053909 (2012).

[59] H. Yu, R. Huber, T. Schwarze, F. Brandl, T. Rapp, P. Berberich, G. Duerr, and D. Grundler, Appl. Phys. Lett. **100**, 262412 (2012).

[60] J. Winter, Phys. Rev. **124**, 452 (1961).

[61] M. Kostylev, J. Appl. Phys. **115**, 233902 (2014).

[62] K. Di, V. L. Zhang, H. S. Lim, S. C. Ng, M. H. Kuok, X. Qiu, and H. Yang, Appl. Phys. Lett. **106**, 052403 (2015).

[63] A. A. Stashkevich, M. Belmeguenai, Y. Roussigné, S. M. Cherif, M. Kostylev, M. Gabor, D. Lacour, C. Tiusan, and M. Hehn, Phys. Rev. B **91**, 214409 (2015).

[64] X. Liu, W. Zhang, M. J. Carter, and G. Xiao, J. Appl. Phys. **110**, 033910 (2011).